Arabian Journal of Chemistry (2023) **16**, 104766

King Saud University

Arabian Journal of Chemistry

www.ksu.edu.sa
www.sciencedirect.com

ORIGINAL ARTICLE

18β-Glycyrrhetinic acid derivative-based metallo-hydrogels with highly selective and sensitive for histidine detection

Kaize Su [a,b], Jiahao Li [a,b], Xiaoyu Guo [a,b], Shengzhu Guo [a,b], Wende Zheng [a,b], Xiaowen Tang [a,b], Duanyu Deng [a,b], Huiji Yang [c], Wing-Leung Wong [d], Song Ang [a,b,*], Kun Zhang [a,b,*], Panpan Wu [a,b,*]

[a] *School of Biotechnology and Health Sciences, Wuyi University, Jiangmen 529020, PR China*
[b] *International Healthcare Innovation Institute (Jiangmen), Jiangmen 529040, PR China*
[c] *College of Chemistry, Beijing Normal University, Beijing 100875, PR China*
[d] *The State Key Laboratory of Chemical Biology and Drug Discovery, Department of Applied Biology and Chemical Technology, The Hong Kong Polytechnic University, Hung Hom, Kowloon, Hong Kong, PR China*

Received 30 November 2022; accepted 27 February 2023
Available online 8 March 2023

KEYWORDS

18β-Glycyrrhetinic acid;
Derivative;
Metallo-hydrogel;
Histidine;
Detection

Abstract Quantitative detection of His has aroused great interest in disease diagnosis since abnormal histidine (His) metabolism would cause a variety of serious diseases. However, exploiting a strategy with facile, highly selective, sensitive sensing and low-cost to monitor His remains a challenge. In this study, a series of novel metallo-hydrogels were successfully constructed, which were composed of 18β-glycyrrhetinic acid (**GA**) derivative (**GA-O-09**) with rare earth metal ions (Ce^{3+}, Tb^{3+}, Eu^{3+} and La^{3+}). In addition, these metallo-hydrogels possessed excellent thermodynamics stability with the gel melting temperature (T_{gel}) ranging from 62.4 ± 0.49 °C to 67.4 ± 0.49 °C and remarkable pH stability over a range of pH values of 3–10. Interestingly, the Histidine (His)-loaded **GA-O-09/Eu^{3+}** hydrogel and the His-loaded **GA-O-09/La^{3+}** hydrogel displayed extraordinary fluorescence enhancement, in which the lowest fluorescence response concentrations (LODs) of the His-loaded **GA-O-09/Eu^{3+}** hydrogel and the His-loaded **GA-O-09/La^{3+}** hydrogel were 1.14×10^{-8} and 1.07×10^{-8} M, respectively. Therefore, the result showed that the study of the **GA-O-09/Eu^{3+}** and **GA-O-09/La^{3+}** hydrogels could provide a potential application for highly selective and sensitive detection for His.

* Corresponding authors.
E-mail addresses: jnuangsong@126.com (S. Ang), kzhang@gdut.edu.cn (K. Zhang), wyuchemwpp@126.com (P. Wu).

https://doi.org/10.1016/j.arabjc.2023.104766
1878-5352 © 2023 The Author(s). Published by Elsevier B.V. on behalf of King Saud University.

1. Introduction

Histidine (His) plays an essential role in human physiological activities as one of the semi-essential amino acids and it can be synthesized in adults or intake from food, such as meat, milk, egg, plants, etc. (Kriengsinyos et al., 2002; Górska-Warsewicz et al., 2018). His is not only a neuromodulator in mammals and acts as a regulator in bio-bases to assist in the transport of metal elements, which can promote the development and perfection of the infant's nervous and immune systems and strengthens physiological metabolic functions (Brosnan and Brosnan, 2020; Holeček, 2020; Yao et al., 2020), but also could be used as a drug or biochemical reagent to treat heart disease, anemia, and rheumatoid arthritis (Guo et al., 1999; Hajdu et al., 2000; Wu et al., 2014). However, the amount of His in human physiological fluids like serum and urine has a certain range from 0.31 to 26.35 $mg{\cdot}mL^{-1}$ (Walters et al., 1980). The insufficiency or profusion deposition of His will lead to suffering from certain diseases. For instance, the inactivation of histidine enzyme in humans can raise the His level and eventually result in histidinemia which can cause hearing loss and memory function as well as speech impairment and mental retardation. It was well known that the profusion of His may susceptible to Parkinson's disease, epilepsy, Friedreich ataxia, etc. On the contrary, the insufficiency of His was due to the insufficient intake of histidine-containing foods or disorders of the histidine metabolic system, which may be vulnerable to AIDS, and chronic kidney disease. (Watanabe et al., 2008; Verri et al., 2009; Prasad et al., 2011; Hu et al., 2014). Hence, it is important to exploit a highly selective and sensitive sensing strategy to monitor whether abnormal metabolism of the His.

Over the past few decades, a wide range of analytical methods had been exploited to detect the content of His, such as liquid chromatography (Wadud et al., 2002), resonance light scattering (Sun et al., 2012b), capillary electrophoresis (Zhou et al., 2010), mass spectrometry (Furuta et al., 1992), etc. However, these techniques typically have some drawbacks, such as low selectivity and sensitivity, time-consuming, complex preprocessing procedures, high cost, and so on (Chen et al., 2018). In recent years, some novel analytical methods based on fluorescent (Azath and Pitchumani, 2013), colorimetric (Xiong et al., 2008), and electrochemical voltammetry (Parthasarathy et al., 2011) had been exploited. For instance, one novel visual detection of histidine assay was explored by utilizing histidine to compete with Murexide for binding with Ni^{2+} resulted in a change in indicator color (Sun et al., 2012a). A logic gate system for the detection of histidine and cysteine were designed by using their specifically interact with copper ions and selectively quench the fluorescence emission of CuNCs (Gu and Cao, 2018). The gold/copper nanocluster (Au/Cu NCs) was applied for the detection of His selectively and sensitively due to the His could trigger the nanocluster to turn on fluorescence (Cai et al., 2020). As an emerging and highly regarded material, the hydrogels with unique 3D cross-link network, biodegradability, and biocompatibility were widely used in multidisciplinary fields in recent years, such as tissue engineering (Zhu and Marchant, 2011; Ghanbari et al., 2022), agriculture (Qu and Luo, 2020), sensors (Bai et al., 2020; Bai et al., 2021), biomedical (Ahmad et al., 2020; Mahmood et al., 2022), and so on. For example, LiCl was polymerized with polyacrylamide (PAM) and hydroxypropyl methyl cellulose (HPMC) by using the one-step photopolymerization approach to form a multifunctional ion-conductive hydrogel, this hydrogel was expected to be widely used as an advanced sensing device (Qin et al., 2022). By mixing the methacrylate silk fibroin (SFMA), glycyrrhizic acid (GA) and Zn^{2+}, a novel self-assembly hydrogel with immunomodulatory properties was prepared, this hydrogel served as a promising dressing for the management of diabetic wounds (Qian et al., 2022). One self-assembled chitosan (CS)-based composite hydrogels were designed by doping GA solution with other components, this hydrogel exhibited excellent adsorption performance for dyes in water and provided a new strategy for wastewater treatment (Wang et al., 2020).

However, the selective recognition of amino acids by hydrogels has been rarely reported (Liu et al., 2019b) and it remains a challenge. **GA-O-09**, as one of 18β-Glycyrrhetinic acid-derived has been confirmed that its unique ability to form a hydrogel by rapid self-assembly (Guo et al., 2021b). In this study, a novel series of metallo-hydrogels were constructed which were composed of 18β-glycyrrhetinic acid (**GA**) derivative (**GA-O-09**) with rare earth metal ions (Ce^{3+}, Tb^{3+}, Eu^{3+} and La^{3+}). The critical parameters related to the stabilities of the **GA-O-09/M^{3+}** (**M^{3+}** = **Ce^{3+}**, **Tb^{3+}**, **Eu^{3+}** and **La^{3+}**) hydrogels such as pH and thermodynamics were studied. Then, the fluorescence intensity of the amino acids-loaded **GA-O-09/M^{3+}** hydrogels was detected. Interestingly, the **GA-O-09/Eu^{3+}** and **GA-O-09/La^{3+}** hydrogels loading His showed remarkable fluorescent response (Xu et al., 2022), and the SEM and FT-IR were employed to explore the possible mechanism of the hydrogels selectively recognizing to His. Moreover, the lowest fluorescence response concentrations (LODs) (Lin et al., 2019a; Liu et al., 2019a) values of His-loaded hydrogels also had been calculated by the fluorescence titration assay, respectively.

2. Materials and methods

2.1. Materials

18β-Glycyrrhetinic acid (GA), 6-trifluoromethylpyridine-3-formaldehyde, and all amino acids were obtained from Sigma-Aldrich Ltd. (America). Europium nitrate, cerous nitrate, lanthanum nitrate, and terbium nitrate were procured from Promega Biotech Co., Ltd. (Beijing, China). All other chemicals used were of analytical grade.

2.2. Apparatus

The fluorescence images were recorded by the FS5 Fluorescence spectrometer (Edinburgh, UK). Fourier transforms infrared (FT-IR) spectra were conducted with an IRAffinity-1S FT-IR spectrometer (Shimadzu, Japan). Scanning electron microscopy (SEM) image was obtained using an FE-SEM 5000 electron microscope (Hitachi, Japan). The test of rheological properties was conducted with MCR 702 MultiDrive Rheometer (Anton Paar, Austria). Energy dispersive spectrometer (EDS) elemental mapping was obtained by using Bruker EDS QUANTAX (Bruker, Germany). The powder X-ray diffraction (PXRD) image was obtained with D8 VENTURE QUEST XRD (Bruker, Germany). Brunauer Emmett

Teller (BET) data was measured by using BSD-660 Physical Adsorption Analyzer (BSD, China). The surface contact angel was measured by CA200 automatic type optical contact angle measuring instrument (Beidou, China).

2.3. Preparation of metallo-hydrogels

The method of synthesizing **GA-O-09** (Scheme S1) has been described in detail in previous study (Guo et al., 2021b). Firstly, **GA-O-09** (15.00 mg) was dissolved in ethanol (0.52 mL) to form a **GA-O-09** ethanol solution. Then, the solution was heated at 50 °C for 1 min with ultrasonic simultaneously. Secondly, one equivalent of the europium nitrate (10.71 mg), cerous nitrate (10.42 mg), lanthanum nitrate (7.80 mg), and terbium nitrate (8.28 mg) were dissolved in ultrapure water (0.48 mL) respectively, to afford four kinds of aqueous solutions containing rare earth metal ions. Finally, the four kinds of aqueous solution were added dropwise into the **GA-O-09**-ethanol solution, respectively, and the metallo-hydrogels were obtained.

2.4. Preparation of amino acids-loaded metallo-hydrogels

lysine (Lys), Asparagine (Asn), histidine (His), cysteine (Cys), tryptophan (Trp), arginine (Arg), valine (Val), aspartic acid (Asp), tyrosine (Tyr), leucine (Leu), glutamic acid (Glu), methionine (Met), alanine (Ala), isoleucine (Ile), glutamine (Gln), threonine (Thr), proline (Pro), glycine (Gly), phenylalanine (Phe) or serine (Ser), of the same equivalents of **GA-O-09** were dissolved in ultrapure water (0.48 mL), respectively, and formed different solutions containing amino acids and **GA-O-09**. The hydrogels were constructed by repeating the above steps of the metallo-hydrogels.

2.5. The pH stability test of the hydrogels

Firstly, one equivalent of the rare earth metal nitrates was dissolved in ultrapure water (0.48 mL) and the desired pH values (range from 1 to 12) were achieved by adding trace amounts of 0.01 M HCl and 0.01 M NaOH solutions. Then the aqueous solution (0.52 mL) was added dropwise into the **GA-O-09**-ethanol solution entirely to form the hydrogels, the pH stability of the hydrogel was determined by inverting the test tube.

2.6. The thermodynamic stability test of the hydrogels

A series of **GA-O-09/M^{3+}** (**M^{3+}** = **Ce^{3+}**, **Tb^{3+}**, **Eu^{3+}** and **La^{3+}**) hydrogels were prepared in 3 mL sample bottles, respectively. Then, placed these hydrogels in a water bath heating device for heating gradually and stopped until the gel collapsed, and recorded the concentration of hydrogel and the sol–gel phase transition temperatures (T_{gel}).

2.7. His detection in human urine samples

Firstly, three healthy volunteers were randomly selected and the then fresh urine was collected from them (Wang and Fan, 2018). The urine was filtered through the membrane and the filtrate was mixed with acetonitrile (5:1, V/V) to precipitate the proteins, Then, the supernatant was collected after being centrifuged at 5000 r/min for 5 mins, and diluted 100 times with 0.01 M PBS buffer. Subsequently, the above steps for the preparation of metallo-hydrogels were repeated to prepare the **GA-O-09/M^{3+}** hydrogels with different diluted urine solutions instead of ultrapure water.

3. Results and discussion

3.1. Preparation and characterization of the metallo-hydrogels

The **GA-O-09/M^{3+}** (**M^{3+}** = **Ce^{3+}**, **Tb^{3+}**, **Eu^{3+}** and **La^{3+}**) hydrogels were prepared and characterized by the SEM, FT-IR, BET, and Surface contact angel test. As shown in the SEM images (Fig. 1a-1d and S1), the **GA-O-09/M^{3+}** hydrogels (Fig. 1a-1d) existed with more compact orderly rod structures than the **GA-O-09** hydrogel (Fig. S1) after being freeze-dried, it was attributed to the strong coordination between metal ions and pyridine group in **GA-O-09,** and the metal ions served the hydrogel network more compact orderly rod structures (Guo et al., 2021b; Guo et al., 2022). The FT-IR image (Fig. 1e and S2) displayed the absorption peaks of the carbonyl group (C = O) in **GA-O-09** moved from 1740 and 1650 cm^{-1} to 1720 and 1640 cm^{-1} after the self-assembled hydrogels formed. These results also indicated that hydrogen bonds might be formed between the carbonyl groups and the molecule of water in these assembly gels (Liu et al., 2019c; Guo et al., 2022). Moreover, the absorption peaks did not change between **GA-O-09** and **GA-O-09/M^{3+}** hydrogels as shown in Fig. 1e, which also suggested that the hydrogen bonds were undistorted. BET test (Table S1) indicated that the BET surface area of the **GA-O-09** hydrogel (14.57 m^2/g) was lower than the **GA-O-09/Eu^{3+}** (17.68 m^2/g) and **GA-O-09/La^{3+}** (17.81 m^2/g) hydrogels and the average pore diameter the **GA-O-09** hydrogel (16.08 nm) was higher than the **GA-O-09/Eu^{3+}** (15.21 nm) and **GA-O-09/La^{3+}** hydrogels (15.48 nm), which may due to the more compact orderly hydrogel network in **GA-O-09/M^{3+}** hydrogels than in **GA-O-09** hydrogel (Maiti et al., 2004). Surface contact angel test (Fig. S3) displayed that there is no significant change in the water contact angle of **GA-O-09** hydrogel and **GA-O-09/M^{3+}** hydrogels (**M^{3+}** = **Eu^{3+}** and **La^{3+}**), all of them were around 130°, which also indicated that they were hydrophobic. (Yang et al., 2022).

Besides, the **GA-O-09/M^{3+}** (**M^{3+}** = **Eu^{3+}**, **La^{3+}**) hydrogels were chosen to make the energy dispersive spectrometer (EDS) elemental mapping images and powder X-ray diffraction (PXRD) images. Fig. 1f and S4 showed that the main elementals (C, O, N, F, Eu and La) were distributed in hydrogels uniformly and obviously. Therefore, it was inferred that the lanthanide ions were well incorporated within the gel network. The powder XRD images (Fig. S5) showed the peaks of **GA-O-09/Eu^{3+}** at around 2θ = 14.98° and 17.81°, and the peaks of **GA-O-09/La^{3+}** at around 2θ = 14.95° and 17.81°, respectively (Calvo-Castro et al., 2016; Son et al., 2018), which was indicated that the π–π stackings that yield between pyridine groups in **GA-O-09** were the main driving forces for the self-assembly of hydrogels. Furthermore, it was also implied that **GA-O-09/M^{3+}** (**M^{3+}** = **Eu^{3+}**, **La^{3+}**) hydrogels were formed with amorphous phase structures. (Liu et al., 2019c; Guo et al., 2021a; Guo et al., 2021b).

In addition, as shown in Fig. 2, the **GA-O-09/M^{3+}** (**M^{3+}** = **Eu^{3+}**, **La^{3+}**) hydrogels were chosen for the rheological exper-

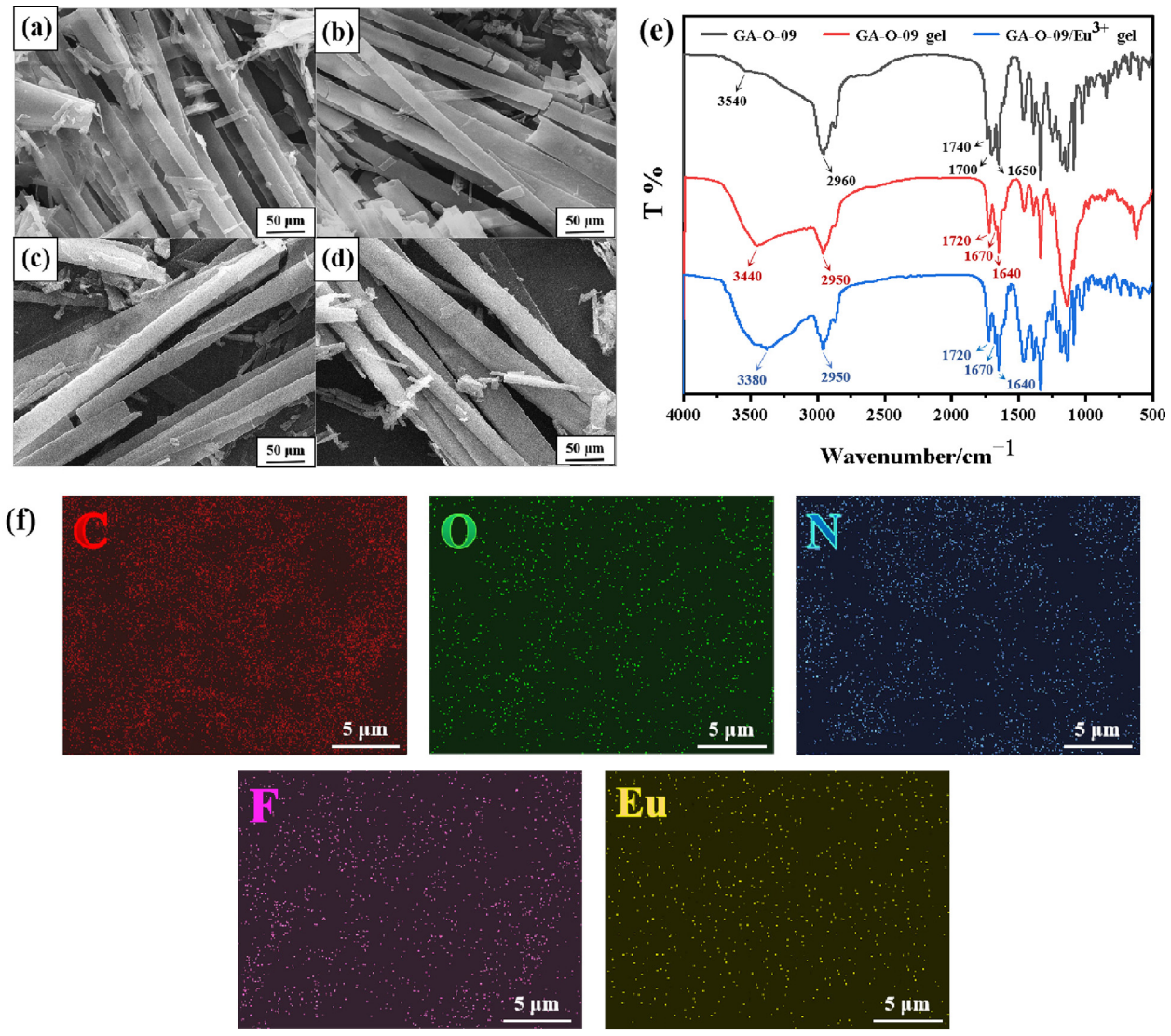

Fig. 1 The SEM images of (a) GA-O-09/Eu^{3+}; (b) GA-O-09/La^{3+}; (c) GA-O-09/Tb^{3+}; (d) GA-O-09/Ce^{3+} hydrogels; (e) the FT-IR spectra of GA-O-09 powder, GA-O-09 and GA-O-09/Eu^{3+} hydrogels; (f) the EDS elemental mapping of GA-O-09/Eu^{3+} hydrogel.

iment to investigate viscoelasticity. The hydrogels exhibited a typical gelatinous behavior since Fig. 2a showed G′ > G″ when the strain amplitude ranged from 0.1 to 100% (Fan et al., 2021; Zeng et al., 2022). When the G′ < G″ at strains that are higher than 100%, the network of hydrogels had been disrupted. The frequency scan (Fig. 2b) also showed the G′ > G″ at the frequency ranging from 0.1 to 100 rad/s which confirmed the gel-like behavior of the hydrogels. Besides, the complex viscosity (η^*) scan (Fig. 2c) reflected that the negatively correlated relationship between complex viscosity and frequency, and the stress–strain curves (Fig. 2d) showed that the hydrogels can withstand at 16 kPa at the strain of 40% approximately.

*3.2. The stability of the **GA-O-09/M^{3+}** hydrogels*

The pH stability of the **GA-O-09/M^{3+}** hydrogels has been studied in a range values of 1 to 12 (Su et al., 2022). Fig. 3 showed that the **GA-O-09/M^{3+}** (**M^{3+}** = **Tb^{3+}**, **Ce^{3+}**, **Eu^{3+}** and **La^{3+}**) hydrogels exhibited pH stability during the range of 3–7, 4–10, 3–10, and 3–10, respectively, which indicated that the excellent pH stability of these metallo-hydrogels except the **GA-O-09/Tb^{3+}** hydrogel.

Subsequently, the sol–gel phase transition temperatures (T_{gel}) were obtained by the test tube inversion method (Liu et al., 2019c) to explore the thermodynamic stability of **GA-O-09/M^{3+}** hydrogels. As listed in Table 1, the values of T_{gel} were increased with increasing the concentration of **GA-O-09/M^{3+}** within a certain range (from 12.5 to 17.0 mg·mL^{-1}), and the T_{gel} of **GA-O-09/M^{3+}** (**M^{3+}** = **Eu^{3+}**, **La^{3+}**, **Tb^{3+}** and **Ce^{3+}**) hydrogels were 66.2 ± 0.75 °C, 67.4 ± 0.49 °C, 62.4 ± 0.49 °C, and 62.6 ± 0.49 °C, respectively, in which the concentration of **GA-O-09** was 17.0 mg·mL^{-1}. Interestingly, the T_{gel} tended to be more/less stable when the concentration of **GA-O-09/M^{3+}** higher than that of 17.0 mg·mL^{-1}. Besides, the minimum gel concentrations of these hydrogels

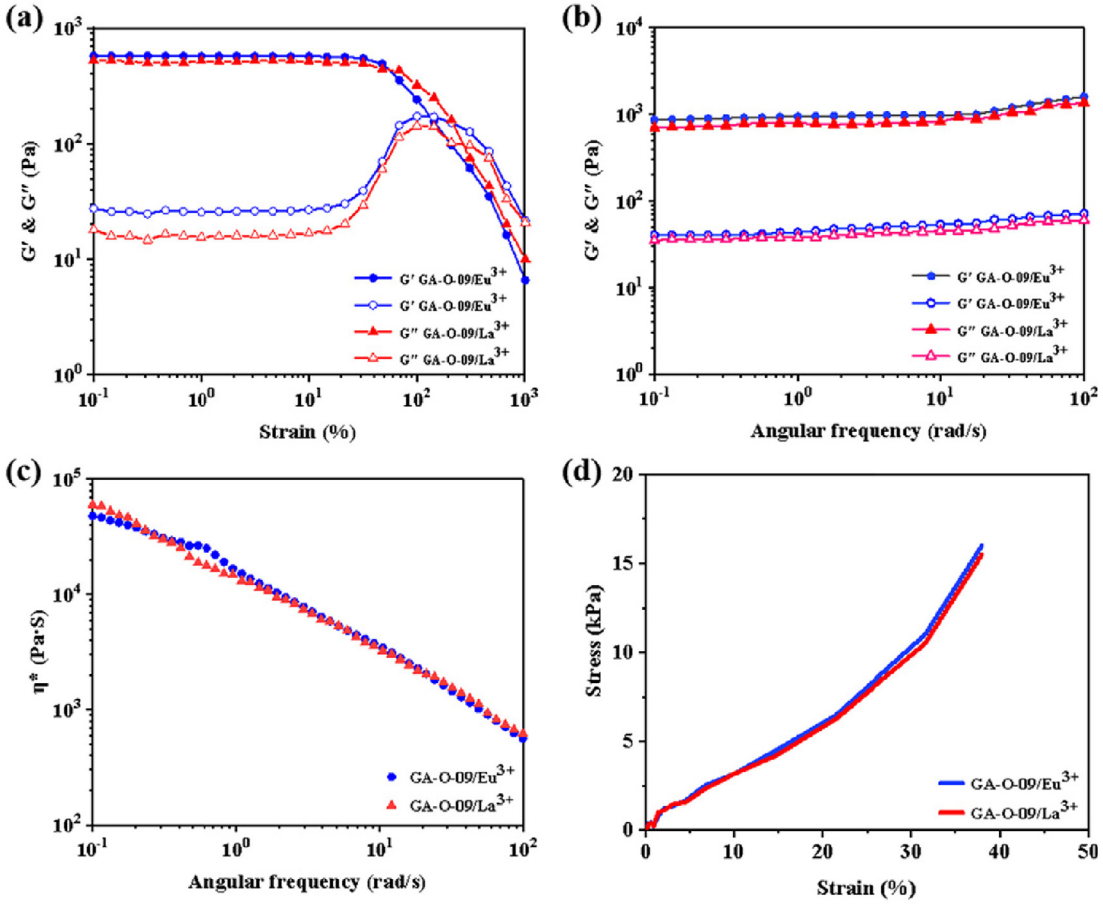

Fig. 2 The rheology test of the GA-O-09/M^{3+} (M^{3+} = Eu^{3+} and La^{3+}) hydrogels: (a) amplitude scan; (b) frequency scan; (c) complex viscosity (η^*) scan; (d) stress–strain curves.

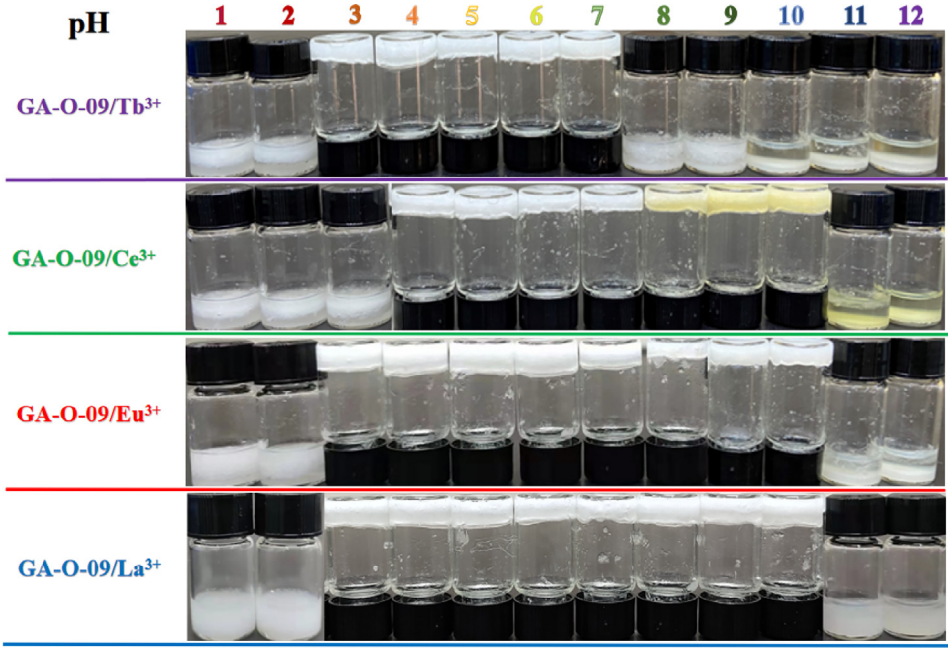

Fig. 3 The stability of the GA-O-09/M^{3+} hydrogels at varied pH values.

Table 1 Corresponding to T_{gel} at different concentrations of **GA-O-09/M^{3+}**.

run	**GA-O-09/Eu^{3+}**		**GA-O-09/Ce^{3+}**		**GA-O-09/Tb^{3+}**		**GA-O-09/La^{3+}**	
	[C] ($mg{\cdot}mL^{-1}$)	T_{gel} (°C)	[C] ($mg{\cdot}mL^{-1}$)	T_{gel} (°C)	[C] ($mg{\cdot}mL^{-1}$)	T_{gel} (°C)	[C] ($mg{\cdot}mL^{-1}$)	T_{gel} (°C)
1	ND	ND	ND	ND	12.5	55.2 ± 0.49	ND	ND
2	13.0	59.6 ± 0.49	13.0	54.8 ± 0.40	13.0	59.6 ± 0.49	13.0	54.8 ± 0.40
3	13.5	60.0 ± 0.63	13.5	56.6 ± 0.49	13.5	60.0 ± 0.63	13.5	56.6 ± 0.49
4	14.0	61.4 ± 0.49	14.0	57.8 ± 0.40	14.0	61.4 ± 0.49	14.0	57.8 ± 0.40
5	14.5	63.4 ± 0.49	14.5	59.2 ± 0.40	14.5	63.4 ± 0.49	14.5	59.2 ± 0.40
6	15.0	64.8 ± 0.40	15.0	60.8 ± 0.47	15.0	64.8 ± 0.40	15.0	60.8 ± 0.47
7	15.5	65.4 ± 0.49	15.5	61.6 ± 0.49	15.5	65.4 ± 0.49	15.5	61.6 ± 0.49
8	16.0	66.2 ± 0.40	16.0	62.0 ± 0.63	16.0	66.2 ± 0.40	16.0	62.0 ± 0.63
9	17.0	66.2 ± 0.75	17.0	62.6 ± 0.49	17.0	66.2 ± 0.75	17.0	62.6 ± 0.49
10	18.0	66.0 ± 0.63	18.0	62.4 ± 0.49	18.0	66.0 ± 0.63	18.0	62.4 ± 0.49
11	19.0	66.2 ± 0.40	19.0	62.2 ± 0.75	19.0	66.2 ± 0.40	19.0	62.2 ± 0.75

[C]: concentration of **GA-O-09**; ND: not detected; T_{gel}: the melting temperature.

were calculated and illustrated in the Table 1 ranging from 1.25 to 1.30 wt%, which were close to the reported super hydrogels (Liu et al., 2019c).

Moreover, Fig. S5 displayed the gel–sol phase change and Van't Hoff plot diagram (Javed et al., 2022), the thermodynamic parameters were calculated in formulas Equations (1) and (2) that can be expressed as:

$$\Delta G = -RT\ln C \tag{1}$$

$$\ln C = -\Delta H/RT - \Delta S/R \tag{2}$$

Where T = 298 K, R = 8.314 $J{\cdot}mol^{-1}{\cdot}K^{-1}$, Δ H was obtained according to the slope of Van't Hoff plot, Δ S was obtained according to the intercept, Δ G was obtained according to Gibbs function.

The comprehensive interpretation of Fig. S6, showed that the ΔG values of the **GA-O-09/M^{3+}** (**M^{3+} = Eu^{3+}**, **La^{3+}**, **Tb^{3+}** and **Ce^{3+}**) hydrogels were 11.43, 12.27, 12.40, and 12.42 $kJ{\cdot}mol^{-1}$, respectively. The comparison indicated that the **GA-O-09/M^{3+}** hydrogels had excellent thermodynamic stability with the positive values of the ΔG, and also the lowest ΔG values revealed the reason why the T_{gel} of **GA-O-09/Eu^{3+}** hydrogel (67.4 ± 0.49 °C) was higher than others at a concentration of 17.0 $mg{\cdot}mL^{-1}$, which meant the **GA-O-09/Eu^{3+}** hydrogel displayed the best thermodynamics stability.

*3.3. The fluorescence detection of amino acids-loaded **GA-O-09/M^{3+}** hydrogels*

The **GA-O-09** and **GA-O-09/M^{3+}** hydrogels were prepared and remained in an inverted test glass cuvette. Then their fluorescence intensity was recorded at 300 nm due to both **GA-O-09** and **GA-O-09/M^{3+}** (**M^{3+} = Eu^{3+}**, **La^{3+}**, **Tb^{3+}** and **Ce^{3+}**) hydrogels having the strongest UV absorption peaks around this wavelength (Fig. S7a). The fluorescence emission spectra of the **GA-O-09** and **GA-O-09/M^{3+}** hydrogels exhibited a maximum peak of around 600 nm upon excitation at 300 nm.

As shown in Fig. 4a and 4b, a series of amino acids-loaded **GA-O-09/M^{3+}** hydrogels were constructed with then their changes in fluorescence intensity were verified during the selective recognition of amino acids. The remarkable fluorescence enhancements of the His-, Lys-, and Arg-loaded **GA-O-09/Eu^{3+}** hydrogels were observed. Interestingly, both the His-loaded **GA-O-09/Eu^{3+}** hydrogel and the His-loaded **GA-O-09/Eu^{3+}** hydrogel displayed the most remarkable fluorescence enhancement upon excitation at 300 nm. Besides, the specific selectivity of the **GA-O-09/M^{3+}** (**M^{3+} = Eu^{3+}**, **La^{3+}**) hydrogels for His was further verified by competitive experiments (Fig. 4c, 4d). 1.0 equiv. His and 1.0 equiv. competitive amino acids were loaded to the hydrogels, respectively. The corresponding fluorescence intensities of hydrogels indicated that there was no obvious interference to recognize the His selectively while other competitive amino acids were presented.

Meanwhile, 365 nm UV lamp was treated as the most common detection wavelength, which was attempted to irradiate the **GA-O-09** and **GA-O-09/M^{3+}** hydrogels loaded with histidine in this study according to the previous study (Liu et al., 2019c). Interestingly, although 365 nm was not the optimal absorption wavelength for detection, the **GA-O-09** and **GA-O-09/M^{3+}** hydrogels emitted green fluorescence (Fig. S7b) and the fluorescence emission color altered from faint green to pink, purple, and cyan while the **GA-O-09/Eu^{3+}** hydrogel loaded 1.0 equiv. His, Lys, and Arg, respectively. However, when His, Arg, and Lys were added to **GA-O-09/La^{3+}** hydrogel, the fluorescence emission color only altered from faint green to cyanine, but the His-loaded **GA-O-09/La^{3+}** hydrogel also displayed the most remarkable fluorescence enhancement than the others.

3.4. The mechanism of selective recognition for His

The possible mechanism of **GA-O-09/M^{3+}** hydrogels selective to recognize His (Fig. 5a) was explored. Fig. 5b showed that the hydroxyl group (–OH) of the **GA-O-09/Eu^{3+}** hydrogels shifted to 3421, 2956 cm^{-1} from 3380, 2950 cm^{-1}, and the carboxyl group (C = O) of the **GA-O-09/Eu^{3+}** hydrogels shifted to 1726, 1647 cm^{-1} from 1720, 1670 and 1640 cm^{-1}, respectively. Besides, it was worth noting that the hydroxyl group shifted to 3440, 2964 cm^{-1} and the carboxyl group shifted to 1732, 1649 cm^{-1} when the **GA-O-09/Eu^{3+}** hydrogels loaded His. Fig. 5c also suggested that the hydroxyl group and carboxyl group shifted to 3437 and 2958 cm^{-1}, 1728 and

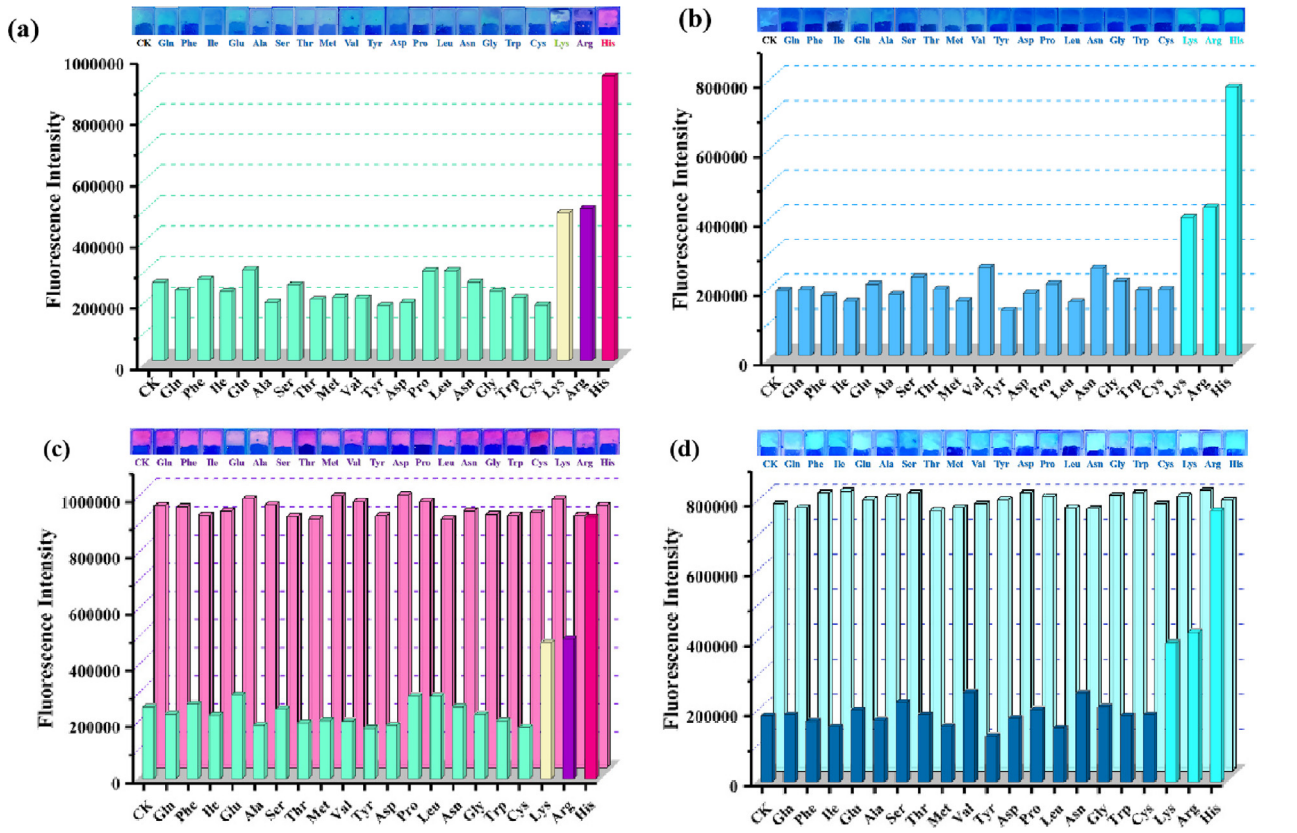

Fig. 4 Photographs of various amino acids-loaded (a) GA-O-09/Eu^{3+} and (b) GA-O-09/La^{3+} hydrogels under 365 nm UV lamp irradiation and the corresponding fluorescence intensity of hydrogels upon excitation at 300 nm; Photographs of (c) GA-O-09/Eu^{3+} and (d) GA-O-09/La^{3+} hydrogels loading 1.0 equiv. His and 1.0 equiv. coexisting amino acids, respectively, under 365 nm UV lamp irradiation and the corresponding fluorescence intensity of hydrogels upon excitation at 300 nm.

1649 cm^{-1} while the **GA-O-09/La^{3+}** hydrogels loaded Arg and Lys, and shifted to 3446, 2964 cm^{-1}, and 1728 cm^{-1}, 1649 cm^{-1} while the **GA-O-09/La^{3+}** hydrogels loaded the His. In summary, the FT-IR characterization indicated that the hydrogen-bonding interactions and electrostatic interactions were generated between carboxylic acid groups and carbonyl groups on the **GA-O-09** and the amino group on His, Arg, and Lys. Interestingly, His, Arg, and Lys were all the basic amino acids and the hydrogen-bonding interactions and electrostatic interactions were the major driving force that caused electron transfer between these basic amino acids and **GA-O-09/M^{3+}**. Besides, the covalent affinity between the unique imidazole group on His and the pyridine group on the **GA-O-09/M^{3+}** caused further electron transfer and remarkable fluorescence changes, in which the His-loaded **GA-O-09/M^{3+}** (**M^{3+}** = **Eu^{3+}**, **La^{3+}**) hydrogels displayed more remarkable fluorescence enhancement than the others.

As displayed in Fig. 5d-5i, the amino acid particles were attached to the **GA-O-09/M^{3+}** (**M^{3+}** = **Eu^{3+}**, **La^{3+}**) xerogels, respectively, and the His-, Arg-, Lys-loaded **GA-O-09/M^{3+}** (**M^{3+}** = **Eu^{3+}**, **La^{3+}**) xerogels possessed layered and agminated structures, which were different from the nano rod-like structures of the **GA-O-09/M^{3+}** (**M^{3+}** = **Eu^{3+}**, **La^{3+}**) xerogels. Meanwhile, the coordination interactions between the **GA-O-09/M^{3+}** (**M^{3+}** = **Eu^{3+}**, **La^{3+}**) and amino acids were further supported by the SEM characterization.

3.5. The sensitivity study of His detection

To evaluate the detection sensitivity of the **GA-O-09/M^{3+}** (**M^{3+}** = **Eu^{3+}**, **La^{3+}**) hydrogels for amino acids, His was selected in this study for that more remarkable fluorescence enhancement was observed when the His was loaded by **GA-O-09/La^{3+}** and **GA-O-09/Eu^{3+}** hydrogels. Fig. 6 and S8 showed the fluorescence intensity was enhanced upon excitation at 300 nm, and 365 nm respectively, and the position of the emission peak shifted from short wavelength to long wavelength (red-shifted) while the hydrogels loaded 1.0 equiv. His. The insets in Fig. S8a and S8b displayed corresponding emission colors change of hydrogel under 365 nm UV lamp irradiation.

Furthermore, the fluorescence titration experiments were investigated to monitor the changes in the fluorescence intensity for different equiv. His (ranging from 0.0 to 1.0 equiv.) loaded by **GA-O-09/M^{3+}** (**M^{3+}** = **Eu^{3+}**, **La^{3+}**) hydrogels, respectively (Fig. 6c, 6d). The results indicated that the fluorescence was enhanced with the increasing of the His concentration, which further confirmed the existence of electron transfer between His and **GA-O-09/M^{3+}** and which caused the change of the emission colors of hydrogel to change. In addition, the LODs was calculated by using the 3 σ/m method, where σ is the standard deviation of the blank and m is the slope of the calibration plot. (Committee, 1987; Nafaâ et al.,

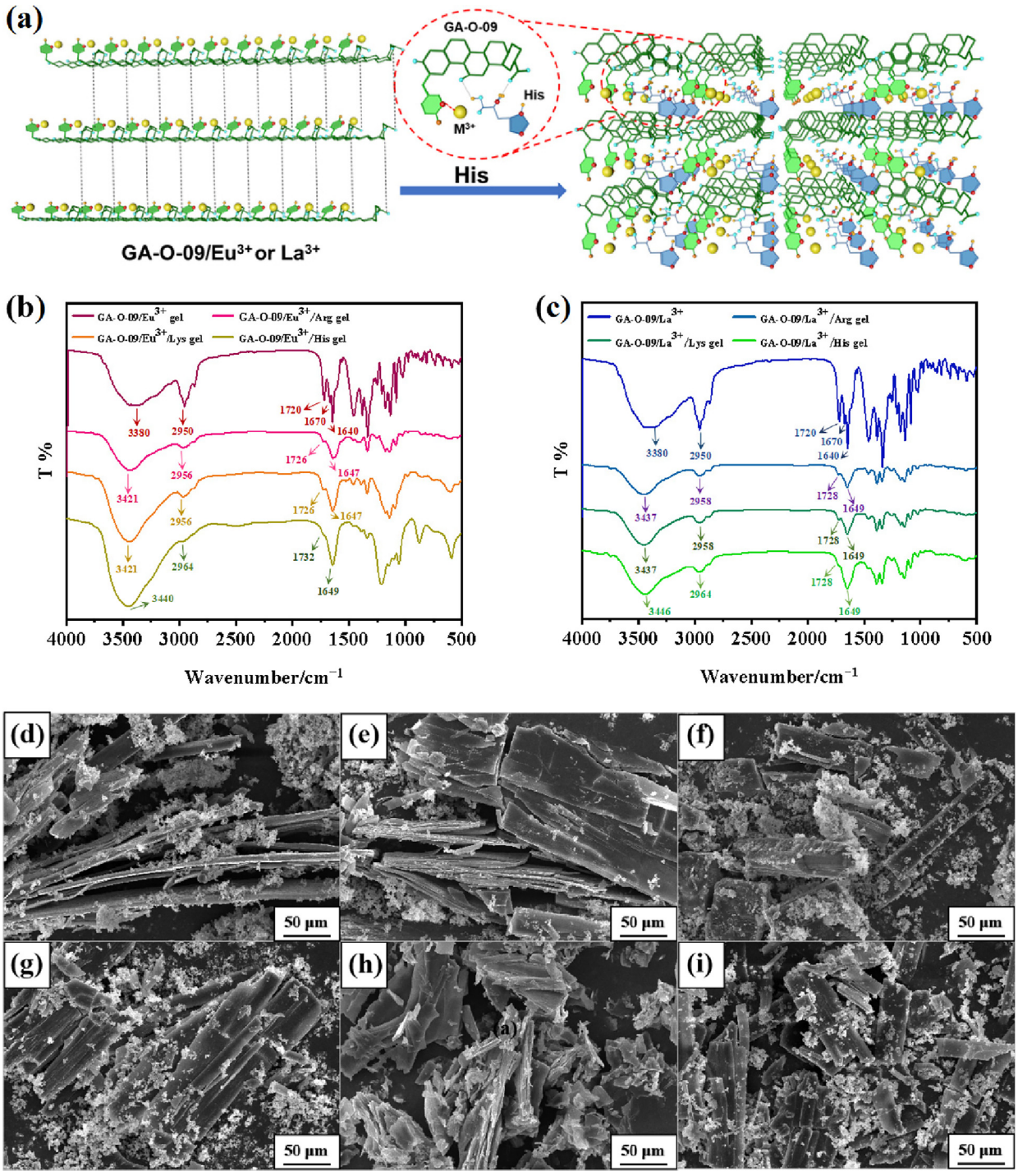

Fig. 5 (a) The possible mechanism of the hydrogels' selective recognition for His; Infrared spectra of (b) GA-O-09/Eu^{3+} and GA-O-09/La^{3+} hydrogels loaded His, Arg, and Lys, respectively; (c) GA-O-09/La^{3+} and GA-O-09/Eu^{3+} hydrogels loaded His, Arg and Lys, respectively; the SEMs of (d) the His-loaded GA-O-09/Eu^{3+} hydrogel; (e) the Arg-loaded GA-O-09/Eu^{3+} hydrogel; (f) the Lys-loaded GA-O-09/Eu^{3+} hydrogel; (g) the His-loaded GA-O-09/La^{3+} hydrogel; (h) the Arg-loaded GA-O-09/La^{3+} hydrogel; (i) the Lys-loaded GA-O-09/La^{3+} hydrogel.

2003; Hua et al., 2017; Lin et al., 2019b; Liu et al., 2019a), and the calculation formulas Equations S1 to S4 were represented in the supplementary material.

As shown in Fig. 6e and 6f, the LODs of **GA-O-09/Eu^{3+}** and **GA-O-09/La^{3+}** hydrogels for His were 1.14 × 10^{-8} M and 1.07 × 10^{-8} M, respectively. Compared to the calculated LODs reported (Table 2), the hydrogels displayed more remarkable selectivity and sensitivity than the others.

Furthermore, the pH and thermodynamic stability of the His-loaded **GA-O-09/M^{3+}** (**M^{3+}** = **Eu^{3+}**, **La^{3+}**) hydrogels were explored. The result indicated the His-loaded hydrogels still exhibited excellent pH stability over a range of 4–10 and

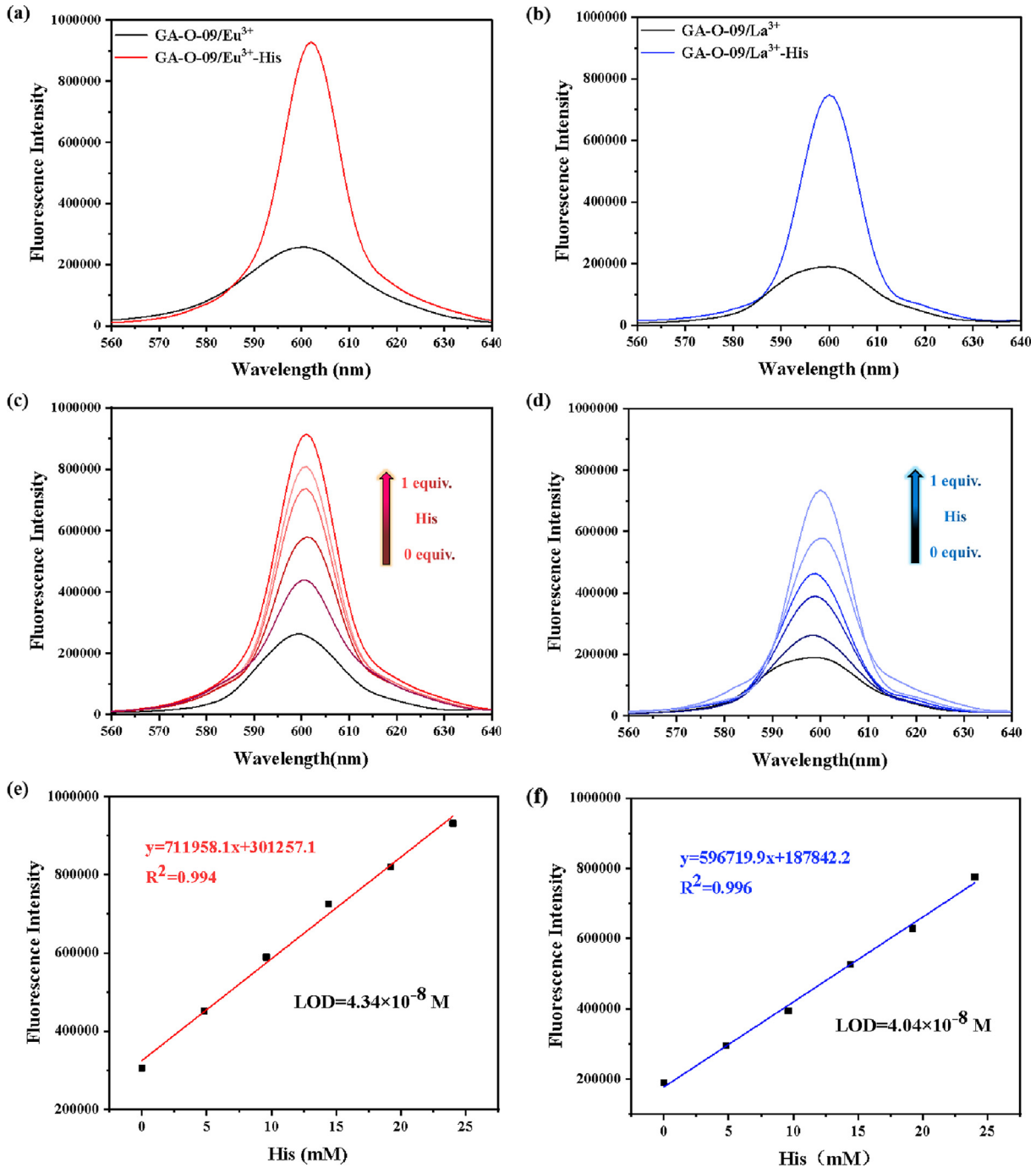

Fig. 6 Comparison of fluorescence intensity between (a) GA-O-09/Eu^{3+} and (b) GA-O-09/La^{3+} hydrogels prepared with 1.0 equiv. of His or without His upon excitation at 300 nm, respectively. The fluorescence intensity of (c) GA-O-09/Eu^{3+} and (d) GA-O-09/La^{3+} hydrogels which were added with different equivalents of His upon excitation at 300 nm, respectively; the fluorescence titration linear range and the LODs of (e) GA-O-09/Eu^{3+} and (f) GA-O-09/La^{3+} hydrogels loading His.

3–9, respectively (Fig. S9), and the thermodynamic stability were not significantly affected with the addition of His (Table S2).

3.6. The determination of His in human urine samples

To further evaluate the practical value of this study, His of human urine samples were detected and analysed (Gu et al., 2018; Gu and Cao, 2018). As shown in Table 3, the concentration of His in the tested urine sample was 834 μM (the concentrations of Founds in Table 3 multiplied by 100), which was within the normal range of His in human urine (the normal level of His was 130–2100 μM in urine) (Sun et al., 2012b). Meanwhile, a series of known concentrations (5, 10, 20, and 50 μM) of His were the spiked respectively to the samples. The result showed that the high recoveries of spiked His ranged from 99.7% to 103.8% and the low relative standard deviations (RSDs) were between 0.8% and 1.9%, which indicated

Table 2 Comparison of the LODs of **GA-O-09/Eu^{3+}** and **GA-O-09/La^{3+}** hydrogels loading His with those of previously studied.

Method	Material	LODs (M)	Reference
Fluorescent	Polymer nanoparticles	7.00×10^{-8}	(Zhang et al., 2017)
Colorimetric	DNAzyme	5.00×10^{-9}	(Gu et al., 2018)
Luminescent	DNAzyme	3.60×10^{-7}	(Li et al., 2018)
Colorimetric	Murexide	4.00×10^{-7}	(Sun et al., 2012b)
Fluorescent	Copper nanoparticle	5.00×10^{-6}	(Liu et al., 2013)
Electrochemical	DNAzyme	3.00×10^{-7}	(Hu et al., 2012)
Fluorescent	Ag/Au nanoclusters	8.70×10^{-8}	(Sun et al., 2015)
Fluorescent	**GA derivative**	**(1.14–1.07) × 10^{-8}**	**This work**

Table 3 Detection of His in samples.

Sample	Spiked (μM)	Measured (μM)	Recovery (%)	RSD (%, n = 3)
1	0	8.34 ± 0.08	–	0.8
2	5	13.53 ± 0.11	103.8	1.6
3	10	18.38 ± 0.22	100.4	1.9
4	20	28.28 ± 0.28	99.7	1.5
5	50	58.33 ± 0.32	99.9	0.9

that this detection method could be successfully applied for His determination in human urine sample.

4. Conclusion

In this study, a series of **GA-O-09/M^{3+}** (**M^{3+}** = **Ce^{3+}**, **Tb^{3+}**, **Eu^{3+}** and **La^{3+}**) hydrogels were prepared with a low critical gelation concentration ranging from 1.25 to 1.30 wt%. These hydrogels exhibited remarkable pH stability over a wide range (from 3 to 10) and excellent thermodynamics stability ($\Delta G > 0$) with the T_{gel} during the range from 62.4 ± 0.49 °C to 67.4 ± 0.49 °C. The **GA-O-09/Eu^{3+}** and **GA-O-09/La^{3+}** hydrogels showed extraordinary fluorescence enhancements while loading His, Lys, and Arg, respectively. Interestingly, the His-loaded **GA-O-09/Eu^{3+}** and His-loaded **GA-O-09/La^{3+}** hydrogels displayed remarkable fluorescence enhancement, and the LODs of these hydrogels loading His were 1.14×10^{-8} and 1.07×10^{-8} M, respectively. Therefore, these results indicated that the **GA-O-09/Eu^{3+}** and **GA-O-09/La^{3+}** hydrogels could provide a potential method for highly selective and sensitive detection for His.

Acknowledgments

This study was supported by the National Natural Science Foundation of China (No. 81803390, 22077020), Natural Science Foundation of Guangdong Province (No. 2021A1515010221, 2023A1515012904), Hong Kong and Macao Joint Research and Development Foundation of 2021 (No. 2021WGALH09 and PolyU P0038670), and Special Funds for the Cultivation of Guangdong College Students' Scientific and Technological Innovation ("Climbing Program" Special Funds, No. pdjh2022a0523). Special Fund Project of Science and Technology Innovation Strategy of Guangdong Province 2018 and 2020 [No. Jiangke(2018)352 and Jiangke (2020)182]. The authors are also grateful to the Foundation of the Department of Education of Guangdong Province (No. 2020KZDZX1202 and 2022KTSCX144).

Appendix A. Supplementary data

Supplementary data to this article can be found online at https://doi.org/10.1016/j.arabjc.2023.104766.

References

Ahmad, A., Mubarak, N., Naseem, K., Tabassum, H., Rizwan, M., Najda, A., Kashif, M., Bin-Jumah, M., Hussain, A., Shaheen, A., 2020. Recent advancement and development of chitin and chitosan-based nanocomposite for drug delivery: Critical approach to clinical research. Arab. J. Chem. 13 (12), 8935–8964. https://doi.org/10.1016/j.arabjc.2020.10.019.

Azath, I., Pitchumani, K., 2013. Flavone modified-β-cyclodextrin as a highly selective and efficient fluorescent chemosensor for Cu2+ ions and l-histidine. Sensor. Actuat. B-Chem. 188, 59–64. https://doi.org/10.1016/j.snb.2013.07.009.

Bai, J., Wang, R., Ju, M., Zhou, J., Zhang, L., Jiao, T., 2020. Facile preparation and high performance of wearable strain sensors based on ionically cross-linked composite hydrogels. Sci. China Mater. 64 (4), 942–952. https://doi.org/10.1007/s40843-020-1507-0.

Bai, J., Wang, R., Wang, X., Liu, S., Wang, X., Ma, J., Qin, Z., Jiao, T., 2021. Biomineral calcium-ion-mediated conductive hydrogels with high stretchability and self-adhesiveness for sensitive iontronic sensors. Cell Rep. Phys. Sci. 2, (11). https://doi.org/10.1016/j.xcrp.2021.100623 100623.

Brosnan, M., Brosnan, J., 2020. Histidine metabolism and function. J. Nutr. 150 (Supplement_1), 2570S–2575S. https://doi.org/10.1093/jn/nxaa079.

Cai, Y., Wang, J., Liu, C., Yang, S., Zhang, Y., Liu, A., 2020. Histidine-triggered turning-on of gold/copper nanocluster fluorescence for the sensitive and selective detection of histidine. Chem. Commun. 56 (78), 11637–11640. https://doi.org/10.1039/D0CC04819D.

Calvo-Castro, J., Morris, G., Kennedy, A., McHugh, C., 2016. Fluorine Directed Two-Dimensional Cruciform π–π Stacking in Diketopyrrolopyrroles. Cryst. Growth Des. 16 (9), 5385–5393. https://doi.org/10.1021/acs.cgd.6b00887.

Chen, X., Ma, R., Ha, W., Shi, Y., 2018. Direct colorimetric detection of aspartic acid in rat brain based on oriented aggregation of Janus

gold nanoparticle. Sensor. Actuat. B-Chem. 274, 668–675. https://doi.org/10.1016/j.snb.2018.08.008.

Committee, A.M., 1987. Recommendations for the definition, estimation and use of the detection limit. Analyst 112 (2), 199–204. https://doi.org/10.1039/AN9871200199.

Fan, J., Zhong, H., Zhang, X., Yuan, T., Chen, H., Peng, H., 2021. Preparation and characterization of oleanolic acid-based low-molecular-weight supramolecular hydrogels induced by heating. ACS Appl. Mater. Inter. 13 (24), 29130–29136. https://doi.org/10.1021/acsami.1c05800.

Furuta, T., Katayama, M., Shibasaki, H., Kasuya, Y., 1992. Simultaneous determination of stable isotopically labelled L-histidine and urocanic acid in human plasma by stable isotope dilution mass spectrometry. J. Chromatogr. B. 576 (2), 213–219. https://doi.org/10.1016/0378-4347(92)80195-v.

Ghanbari, M., Salavati-Niasari, M., Mohandes, F., Firouzi, Z., 2022. Modified silicon carbide NPs reinforced nanocomposite hydrogels based on alginate-gelatin by with high mechanical properties for tissue engineering. Arab. J. Chem. 15, (1). https://doi.org/10.1016/j.arabjc.2021.103520 103520.

Górska-Warsewicz, H., Laskowski, W., Kulykovets, O., Kudlińska-Chylak, A., Czeczotko, M., Rejman, K., 2018. Food products as sources of protein and amino acids-The case of Poland. Nutrients 10 (12), 1977. https://doi.org/10.3390/nu10121977.

Gu, Z., Cao, Z., 2018. Molecular switch-modulated fluorescent copper nanoclusters for selective and sensitive detection of histidine and cysteine. Anal. Bioanal. Chem. 410 (20), 4991–4999. https://doi.org/10.1007/s00216-018-1149-9.

Gu, P., Zhang, G., Deng, Z., Tang, Z., Zhang, H., Khusbu, F.Y., Wu, K., Chen, M., Ma, C., 2018. A novel label-free colorimetric detection of l-histidine using Cu(2+)-modulated G-quadruplex-based DNAzymes. Spectrochimica Acta A. 203, 195–200. https://doi.org/10.1016/j.saa.2018.05.084.

Guo, S., Chen, S., Cao, N., Zheng, W., Li, D., Sheng, Z., Xu, X., Zhang, Q., Zheng, X., Wu, K., 2021a. A novel 18β-glycyrrhetinic acid derivative supramolecular self-assembly hydrogel with antibacterial activity. J. Mater. Sci. 56 (30), 17254–17267. https://doi.org/10.1007/s10853-021-06396-x.

Guo, S., Fan, Y., Hong, W., Liang, J., Luo, Z., Zheng, W., Li, D., Gan, L., Xu, X., Wu, R., Jin, J., Zheng, X., Wu, P., 2021b. Super-Rapid formation of a novel super-supramolecular hydrogel with excellent antimicrobial activity. Compos. Commun. 28,. https://doi.org/10.1016/j.coco.2021.100955 100955.

Guo, S., Su, K., Yang, H., Zheng, W., Zhang, Z., Ang, S., Zhang, K., Wu, P., 2022. Novel natural glycyrrhetinic acid-derived super metal gel and its highly selective dyes removal. Gels 8 (3), 188. https://doi.org/10.3390/gels8030188.

Guo, C., Xiao, W., Jian, D., Hong, C., 1999. A study on electrochemistry of histidine and its metabolites based on the diazo coupling reaction. Talanta 49 (2), 319–330. https://doi.org/10.1016/S0039-9140(98)00379-8.

Hajdu, J., Neutze, R., Sjögren, T., Edman, K., Szöke, A., Wilmouth, R., Wilmot, C., 2000. Analyzing protein functions in four dimensions. Nat. Struct. Biol. 7 (11), 1006–1012. https://doi.org/10.1038/80911.

Holeček, M., 2020. Histidine in health and disease: metabolism, physiological importance, and use as a supplement. J. Nutr. 12 (3), 848. https://doi.org/10.3390/nu12030848.

Hu, R., Fu, T., Zhang, X., Kong, R., Qiu, L., Liu, Y., Liang, X., Tan, W., Shen, G., Yu, R., 2012. A proximity-dependent surface hybridization strategy for constructing an efficient signal-on electrochemical DNAzyme sensing system. Chem. Commun. 48 (76), 9507–9509. https://doi.org/10.1039/C2CC34848A.

Hu, Y., Wang, Q., Zheng, C., Wu, L., Hou, X., Lv, Y., 2014. Recyclable decoration of amine-functionalized magnetic nanoparticles with Ni(2+) for determination of histidine by photochemical vapor generation atomic spectrometry. Anal. Chem. 86 (1), 842–848. https://doi.org/10.1021/ac403378d.

Hua, Y.-X., Shao, Y., Wang, Y.-W., Peng, Y., 2017. A series of fluorescent and colorimetric chemodosimeters for selective recognition of cyanide based on the FRET mechanism. The Journal of Organic Chemistry 82 (12), 6259–6267. https://doi.org/10.1016/j.dyepig.2012.05.006.

Javed, M., Iqbal, S., Fatima, I., Nadeem, S., Mohyuddin, A., Arif, M., Amjad, A., Shahid, S., Alshammari, F., Alahmdi, M., 2022. Interactions between amino acids and a cationic surfactant in binary solvent system. Colloid Interfac. Sci. 48,. https://doi.org/10.1016/j.colcom.2022.100623 100623.

Kriengsinyos, W., Rafii, M., Wykes, L., Ball, R., Pencharz, P., 2002. Long-term effects of histidine depletion on whole-body protein metabolism in healthy adults. J. Nutr. 132 (11), 3340–3348. https://doi.org/10.1093/jn/132.11.3340.

Li, Z., Zhao, J., Wang, Z., Dai, Z., 2018. Nickel-mediated allosteric manipulation of G-quadruplex DNAzyme for highly selective detection of histidine. Anal. Chim. Acta 1008, 90–95. https://doi.org/10.1016/j.aca.2017.12.040.

Lin, Q., Guan, X.-W., Zhang, Y.-M., Wang, J., Fan, Y.-Q., Yao, H., Wei, T.-B., 2019. Spongy materials based on supramolecular polymer networks for detection and separation of broad-spectrum pollutants. ACS Sustain. Chem. Eng. 7 (17), 14775–14784. https://doi.org/10.1021/acssuschemeng.9b02791.

Liu, J., Fan, Y.-Q., Zhang, Q.-P., Yao, H., Zhang, Y.-M., Wei, T.-B., Lin, Q., 2019. Super metal hydrogels constructed from a simple tripodal gelator and rare earth metal ions and its application in highly selective and ultrasensitive detection of histidine. Soft Matter 15 (5), 999–1004. https://doi.org/10.1039/c8sm02319k.

Liu, J., Fan, Y.-Q., Song, S.-S., Gong, G.-F., Wang, J., Guan, X.-W., Yao, H., Zhang, Y.-M., Wei, T.-B., Lin, Q., 2019a. Aggregation-induced emission supramolecular organic framework (AIE SOF) gels constructed from supramolecular polymer networks based on tripodal pillar [5] arene for fluorescence detection and efficient removal of various analytes. ACS Sustain. Chem. Eng. 7 (14), 11999–12007. https://doi.org/10.1021/acssuschemeng.9b00452.

Liu, Y., Hu, R., Liu, T., Zhang, X., Tan, W., Shen, G., Yu, R., 2013. Label-free dsDNA-Cu NPs-based fluorescent probe for highly sensitive detection of L-histidine. Talanta 107, 402–407. https://doi.org/10.1016/j.talanta.2013.01.038.

Mahmood, A., Patel, D., Hickson, B., DesRochers, J., Hu, X., 2022. Recent progress in biopolymer-based hydrogel materials for biomedical applications. Int. J. Mol. Sci. 23 (3), 1415. https://doi.org/10.3390/ijms23031415.

Maiti, P.K., Cagin, T., Wang, G., Goddard, W.A., 2004. Structure of PAMAM dendrimers: Generations 1 through 11. Macromolecules 37 (16), 6236–6254. https://doi.org/10.1021/ma035629b.

Nafaâ, A., Lotfi, M., Meriem, T., Khaled, B., 2003. Determination of naproxen in pharmaceuticals by differential pulse voltammetry at a platinum electrode. Anal. Chim. Acta 495 (1–2), 69–75. https://doi.org/10.1016/S0003-2670(03)00922-X.

Parthasarathy, S., Long, F., Miller, Y., Xiao, Y., McElheny, D., Thurber, K., Ma, B., Nussinov, R., Ishii, Y., 2011. Molecular-level examination of Cu2+ binding structure for amyloid fibrils of 40-residue Alzheimer's beta by solid-state NMR spectroscopy. J. Am. Chem. Soc. 133 (10), 3390–3400. https://doi.org/10.1021/ja1072178.

Prasad, B., Kumar, D., Madhuri, R., Tiwari, M., 2011. Metal ion mediated imprinting for electrochemical enantioselective sensing of L-histidine at trace level. Biosens. Bioelectron. 28 (1), 117–126. https://doi.org/10.1016/j.bios.2011.07.008.

Qian, Y., Zheng, Y., Jin, J., Wu, X., Xu, K., Dai, M., Niu, Q., Zheng, H., He, X., Shen, J., 2022. Immunoregulation in diabetic wound repair with a photoenhanced glycyrrhizic acid hydrogel scaffold. Adv. Mater. 34 (29), 2200521. https://doi.org/10.1002/adma.202200521.

Qin, Z., Liu, S., Bai, J., Yin, J., Li, N., Jiao, T., 2022. Ionic conductive hydroxypropyl methyl cellulose reinforced hydrogels with extreme stretchability, self-adhesion and anti-freezing ability for highly

sensitive skin-like sensors. Int. J. Biol. Macromol. 220, 90–96. https://doi.org/10.1016/j.ijbiomac.2022.08.055.

Qu, B., Luo, Y., 2020. Chitosan-based hydrogel beads: Preparations, modifications and applications in food and agriculture sectors-A review. Int. J. Biol. Macromol. 152, 437–448. https://doi.org/10.1016/j.ijbiomac.2020.02.240.

Son, S., Kim, J., Song, E., Choi, K., Lee, J., Cho, K., Kim, T., Park, T., 2018. Exploiting π–π stacking for stretchable semiconducting polymers. Macromolecules 51 (7), 2572–2579. https://doi.org/10.1021/acs.macromol.8b00093.

Su, K., Guo, S., Yang, H., Zheng, W., Chen, X., Xu, G., Ang, S., Zhang, K., Wu, P., 2022. Novel Metallo-hydrogels as a two-in-one agent with potent dyes removal and antimicrobial capacity. Colloid Interfac. Sci. 49,. https://doi.org/10.1016/j.colcom.2022.100644 100644.

Sun, S.-K., Tu, K.-X., Yan, X.-P., 2012. An indicator-displacement assay for naked-eye detection and quantification of histidine in human urine. Analyst 137 (9), 2124–2128. https://doi.org/10.1039/c2an35126a.

Sun, J., Yang, F., Zhao, D., Chen, C., Yang, X., 2015. Integrated logic gate for fluorescence turn-on detection of histidine and cysteine based on Ag/Au bimetallic nanoclusters-Cu2+ ensemble. Appl. mater. interf. 7 (12), 6860–6866. https://doi.org/10.1021/acsami.5b00434.

Verri, C., Roz, L., Conte, D., Liloglou, T., Livio, A., Vesin, A., Fabbri, A., Andriani, F., Brambilla, C., Tavecchio, L., Calarco, G., Calabro, E., Mancini, A., Tosi, D., Bossi, P., Field, J.K., Brambilla, E., Sozzi, G., Consortium, E., 2009. Fragile histidine triad gene inactivation in lung cancer: the European Early Lung Cancer project. Am. J. Resp. Crit. Care 179 (5), 396–401. https://doi.org/10.1164/rccm.200807-1153OC.

Wadud, S., Or-Rashid, M., Onodera, R., 2002. Method for determination of histidine in tissues by isocratic high-performance liquid chromatography and its application to the measurement of histidinol dehydrogenase activity in six cattle organs. J. Chromatography B 767 (2), 369–374. https://doi.org/10.1016/S1570-0232(01)00607-9.

Walters, R., Johnson, P., Buck, R., 1980. Histidine ammonia-lyase enzyme electrode for determination of L-histidine. J. Anal. Chem. 52 (11), 1684–1690. https://doi.org/10.1021/ac50061a035.

Wang, Z., Fan, Z., 2018. Cu2+ modulated nitrogen-doped grapheme quantum dots as a turn-off/on fluorescence sensor for the selective detection of histidine in biological fluid. Spectrochim Acta A. 189, 195–201. https://doi.org/10.1016/j.saa.2017.08.003.

Wang, R., Zhang, X., Zhu, J., Bai, J., Gao, L., Liu, S., Jiao, T., 2020. Facile preparation of self-assembled chitosan-based composite hydrogels with enhanced adsorption performances. Colloid. Surface. A. 598,. https://doi.org/10.1016/j.colsurfa.2020.124860 124860.

Watanabe, M., Suliman, M., Qureshi, A., Garcia-Lopez, E., Bárány, P., Heimbürger, O., Stenvinkel, P., Lindholm, B., 2008. Consequences of low plasma histidine in chronic kidney disease patients: associations with inflammation, oxidative stress, and mortality. Am. J. Clin. Nutr. 87 (6), 1860–1866. https://doi.org/10.1007/s004100000161.

Wu, G., Bazer, F., Dai, Z., Li, D., Wang, J., Wu, Z., 2014. Amino acid nutrition in animals: protein synthesis and beyond. Annu. Rev. Anim. Biosci. 2, 387–417. https://doi.org/10.1146/annurev-animal-022513-114113.

Xiong, D., Chen, M., Li, H., 2008. Synthesis of para-sulfonatocalix[4]arene-modified silver nanoparticles as colorimetric histidine probes. Chem. Commun. 7, 880–882. https://doi.org/10.1039/b716270g.

Xu, Z., Li, M., Fang, X., Zhang, L., Ji, L., Liu, Y., Xu, K., Yu, H., 2022. Dual channel detecting of CO in a metal complex gel system: Phase transition and fluorescence enhancement. Colloid Interfac. Sci. 48,. https://doi.org/10.1016/j.colcom.2022.100613 100613.

Yang, J., Li, H., Yi, Z., Liao, M., Qin, Z., 2022. Stable superhydrophobic wood surface constracting by KH580 and nano-Al2O3 on polydopamine coating with two process methods. Colloid. Surface. A 637,. https://doi.org/10.1016/j.colsurfa.2021.128219 128219.

Yao, Z., Liu, H., Liu, Y., Zhang, Q., Diao, Y., Sun, Y., Li, Z.J.M.A., 2020. Fluorimetric determination of histidine by exploiting its inhibitory effect on the oxidation of thiamine by cobalt-containing Prussian Blue nanocubes. 187 (1), 1–7. https://doi.org/10.1007/s00604-019-3930-7.

Zeng, H., Liu, X., Zhang, Z., Song, X., Quan, J., Zheng, J., Shen, Z., Ni, Y., Liu, C., Zhang, Y., 2022. Self-healing, injectable hydrogel based on dual dynamic covalent cross-linking against postoperative abdominal cavity adhesion. Acta Biomater. https://doi.org/10.1016/j.actbio.2022.08.030.

Zhang, Z., Wang, L., Li, G., Ye, B., 2017. Lanthanide coordination polymer nanoparticles as a turn-on fluorescence sensing platform for simultaneous detection of histidine and cysteine. Analyst 142 (10), 1821–1826. https://doi.org/10.1039/C7AN00415J.

Zhou, L., Yan, N., Zhang, H., Zhou, X., Pu, Q., Hu, Z., 2010. Microwave-accelerated derivatization for capillary electrophoresis with laser-induced fluorescence detection: a case study for determination of histidine, 1- and 3-methylhistidine in human urine. Talanta 82 (1), 72–77. https://doi.org/10.1016/j.talanta.2010.03.061.

Zhu, J., Marchant, R., 2011. Design properties of hydrogel tissue-engineering scaffolds. Expert Rev. Med. Devices 8 (5), 607–626. https://doi.org/10.1586/erd.11.27.